A two-phased modelling approach for corrosion-induced concrete cracking and bond deterioration in reinforced concrete

Van Steen, C.; Van Beirendonck, T.; Vrijdaghs, R.; Hendriks, M. A.N.; Verstrynge, E.

DOI
10.1016/j.engstruct.2023.116624

Publication date
2023

Document Version
Final published version

Published in
Engineering Structures

Engineering Structures 294 (2023) 116624

Contents lists available at ScienceDirect

Engineering Structures

journal homepage: www.elsevier.com/locate/engstruct

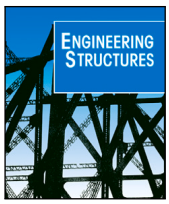

A two-phased modelling approach for corrosion-induced concrete cracking and bond deterioration in reinforced concrete

C. Van Steen [a,*], T. Van Beirendonck [a], R. Vrijdaghs [a], M.A.N. Hendriks [b,c], E. Verstrynge [a]

[a] Department of Civil Engineering, KU Leuven, Leuven, Belgium
[b] Faculty of Civil Engineering and Geosciences, TU Delft, Delft, The Netherlands
[c] Department of Structural Engineering, NTNU, Trondheim, Norway

ARTICLE INFO

Keywords:
Bond
Reinforced concrete
Corrosion
Finite element model

ABSTRACT

Bond deterioration is one of the major consequences of reinforcement corrosion in reinforced concrete (RC) structures. In this paper, a two-phased numerical modelling approach is presented that aims to determine the constitutive behaviour (bond–slip) at the reinforcement-concrete interface at a certain corrosion level. The novelty of the approach is that it consists of a crack model and a bond model, and that the flow of corrosion products into the pores and corrosion-induced cracks as well as the effect of the bonded length and concrete cover are taken into account in the 2D crack model. The resulting expansion of corrosion products from the crack model is used as input in the 3D bond model. The combination of both models leads to a procedure that balances computational time and modelling detail. The model is validated on a substantial amount of experimental pull-out test results. A good agreement is obtained between the experimental data and the models for different corrosion levels in terms of crack width, crack pattern, corrosion-induced bond loss, and failure mode.

1. Introduction

Reinforcement corrosion is an electrochemical process in which steel is dissolved and turned into expansive corrosion products. As the corrosion products occupy a greater volume than the original steel, internal tensile stresses will occur, leading to cracking of the concrete cover. Both concrete cracking and steel section loss have an influence on the bond strength at the reinforcement-concrete interface. In degrading reinforced concrete (RC) structures, bond deterioration is one of the most important damage modes. Studies on small, unconfined samples have shown that the loss of bond strength due to corrosion can go up to 80% while the reduction of the cross section is rather low [1,2].

The bond between steel and concrete allows longitudinal forces to be transferred from the rebar to the surrounding concrete leading to the composite behaviour of reinforced concrete. The interaction between both materials strongly depends on the characteristics of the interface. When strains in the steel are different from strains in the concrete, the rebar can start to slip. The bond strength of ribbed rebars is caused by following mechanisms: adhesion, friction, and mechanical interlocking between the steel ribs and the surrounding concrete. For smooth rebars, only adhesion and friction contribute to the bond resistance. The reinforcement-concrete interaction is typically expressed by a bond–slip or $\tau - \delta$ relation. From pull-out tests on small specimens, it is known that the bond strength increases for low corrosion levels as the formed corrosion products first fill the pores surrounding the rebar which will lead to more confinement. However, the majority of design guidelines omit initial bond strength increase [3]. When the concrete cover cracks, this confinement is lost, leading to a reduced bond strength [4–7]. When stirrups are present, they will provide additional confinement leading to smaller crack widths compared to specimens without stirrups at similar corrosion levels and as such influence the reduction in bond strength [8]. For low corrosion levels, stirrups may help avoiding splitting-type bond failure. Still, a decrease in bond strength can be noticed for larger crack widths [4].

Modelling of the bond behaviour of corroded specimens is challenging as on the one hand the mechanisms of the corrosion process and on the other hand the mechanisms of the composite behaviour of steel and concrete should be taken into account. Simplification of these mechanisms is necessary.

Axisymmetric modelling approaches were for example developed by Berto et al. [9] and Chernin et al. [10]. In the model of Berto et al. [9], the bond behaviour of ribbed rebars is modelled by assigning a $\tau - \delta$ relation to an interface which describes the steel-concrete connection. Two different constitutive models for the interface are investigated:

* Corresponding author.
E-mail address: charlotte.vansteen@kuleuven.be (C. Van Steen).

https://doi.org/10.1016/j.engstruct.2023.116624
Received 14 December 2022; Received in revised form 13 June 2023; Accepted 15 July 2023
Available online 9 August 2023

frictional type and damage type. The former allowed a variation in bond strength and initial stiffness, the latter is based on the $\tau - \delta$ relation obtained from the fib Model Code [3]. The axisymmetric model proposed by Chernin et al. [10] is based on a different approach. A thermal analogy is used to mimic the expansive nature of corrosion products and a Coulomb friction model is assigned to an interface to describe the bond behaviour. Two parameters, the cohesion (c) and the friction coefficient (μ), are adapted for different corrosion levels based on values obtained from the literature. Also the post-peak pull-out behaviour is described by changing the cohesion and friction coefficient in function of the slip. The model is limited to smooth rebars and corrosion levels that do not cause cracking. The advantage of an axisymmetric modelling approach is the reduced calculation time in comparison with 3D models. The bond behaviour is determined by an interface which depends on few parameters. The disadvantage is that corrosion-induced cracks cannot be modelled realistically and non-uniform corrosion is difficult to incorporate.

Extensive work using detailed 3D finite element models has been performed by Lundgren et al. [11–14]. A bond model without corrosion was first developed by Lundgren and Gylltoft [11] taking different failure mechanisms into account such as pull-out failure, splitting failure, and yielding of the rebar. The effect of corrosion was later modelled by adding the expansion of corrosion products in an interface layer [12]. Cracking of the concrete cover was allowed by a smeared cracking approach. The models were enhanced in subsequent publications as it was shown that energy was generated for specific loading–unloading sequences due to an asymmetric stiffness matrix, which was undesirable [13,14]. The bond model was reformulated and became equivalent to a Coulomb friction model. Models were initially calibrated on ribbed rebars, but the parameters can be adapted for smooth rebars [15]. However, the model becomes numerically unstable when extensive cover cracking occurs as the effect of corrosion products penetrating pores (in the so-called corrosion accommodation region (CAR) [16]) and cracks was not taken into account. This was later adapted by Zandi Hanjari et al. [17]. Amleh and Ghosh [18] also used a 3D model with a Coulomb friction model describing the interface. A relation between the contact pressure and concrete cover thickness was derived for uncorroded samples. This contact pressure was reduced with increasing corrosion level representing the formation and propagation of longitudinal cracks. An exponential decay law was assumed for the friction coefficient in relation to the slip for uncorroded samples. The value of the static friction coefficient decreased with rebar mass loss. An initial increase of the bond strength was not taken into account, and neither was the contribution of cohesion. As 3D models with solid elements can be computationally demanding, Grassl and Davies [19] used a computationally efficient lattice modelling approach. However, the calibration of such models is not straightforward and the expansion of corrosion products was a model parameter instead of a material parameter observed from experiments.

It is clear from the literature study that a proper model for the bond–slip relation of corroded RC should include the influence of concrete cover cracking and the confinement reduction, as well as the penetration of corrosion products in pores and cracks which affects the pressure build-up. In addition, the possibility to integrate non-uniform corrosion, various section layouts and rebar types would greatly improve the versatility of the model's application. Finally, computational efficiency may be a hindrance for full 3D models.

To address these challenges, this paper presents a two-phased numerical modelling approach based on the finite element (FE) method, which is validated on experimental data. The aim of the model is to determine the constitutive behaviour (bond–slip) at the reinforcement-concrete interface at a certain corrosion level. The novelty of the proposed approach is that the model is two-phased, meaning that it exists of a crack model and a bond model, which allows to incorporate the required amount of detail to model the complex interacting processes without leading to extensive computational cost. The work also proposes a novel approach to incorporate the effect of confinement for different bonded lengths. Within the scope of the current paper, the model focuses on samples with centrically and eccentrically positioned ribbed rebars without stirrups.

First, the experimental setup and resulting datasets of the cracking and pull-out behaviour of the samples in three test series are briefly discussed, as these experimental findings influence the modelling steps that are taken. Second, the working principle and implementation of the crack model are explained. Third, the implementation of the bond model is presented. Finally, the results of the crack and bond model are discussed and compared with the experimentally observed bond–slip behaviour at various corrosion levels.

2. Experimental program

2.1. Samples and test setups

An extensive experimental program was performed of which a detailed overview is presented in Van Steen et al. [20] and Van Beirendonck et al. [8]. A total of 117 samples were tested having similar dimensions, namely 150 × 150 × 250 mm. The samples varied in rebar type (smooth or ribbed), corrosion level (CL), bond length, cover thickness, and confinement (whether or not stirrups are present).

From this large dataset, only samples with a ribbed rebar and without stirrups are considered in this paper. An overview of these samples and their parameters is given in Table 1. The samples are divided in three test series (TS). The differences between the test series are explained below. Fig. 1 shows a cross-section of the samples. Outside of the bonded length, the rebars were protected from corrosion, so the bonded length is the same as the corroding length.

For TS1, the samples were designed with a bond length of 100 mm. It was noticed during testing that this was too large for the smallest target corrosion level of 1.5% and failure of the rebar was observed.

To avoid failure of the rebar at small corrosion levels, some measures were taken when designing the samples of the second test series. The main difference between TS1 and TS2 is the bond length which was reduced to 42 mm while keeping the other dimensions similar. A rebar diameter of 14 mm instead of 12 mm was used. The force required to pull the rebar out will be smaller due to the smaller bonded length and the force at yielding and failure of the rebar will be higher due to the larger rebar diameter. It was anticipated that increasing the rebar diameter would in this case have a minor effect on the bond strength.

The aim of TS3 was to investigate the effect of a reduced concrete cover. Therefore, the main difference between TS2 and TS3 is the thickness of the concrete cover which was reduced to 30 mm compared to the original 68 mm. It was anticipated that this would have most effect on the lower corrosion levels and that CL3 would lead to a larger crack width and a lower bond strength. Therefore, only two corrosion levels were tested besides the reference samples for TS3.

The samples were corroded to a target corrosion level in an accelerated corrosion setup. A direct current with a current density of 100 μA/cm^2 was applied on the rebar. The rebar served as an anode. A stainless steel plate was used as a cathode. The sample was partially immersed in a 5% sodium chloride solution. The number of corrosion days was calculated using Faraday's law. However, it should be noted that the obtained corrosion level can deviate from the target corrosion level as Faraday's law assumes that all current is applied to dissolve iron in the electrochemical reaction, which is not the case. For a more detailed description of the corrosion setup, the reader is referred to Van Steen et al. [20].

A typical pull-out setup is shown in Fig. 2. A testing machine with a capacity of 100 kN was used. The sample was placed in a steel frame. The rebar was fixed at the bottom while the head of the testing machine was moving upwards. All samples were tested in a displacement-controlled regime with a loading speed of 0.3 mm/min

Table 1
Overview of the design parameters of the samples considered in this paper.

Test series (TS)	Target corrosion level [%]	Rebar diameter [mm]	Bond length [mm]	Concrete cover [mm]	Number of samples
TS1	0 (CL0)	12	100	69	3
	1.5 (CL1)	12	100	69	3
	5 (CL2)	12	100	69	3
	10 (CL3)	12	100	69	3
TS2	0 (CL0)	14	42	68	3
	1 (CL1)	14	42	68	3
	5 (CL2)	14	42	68	3
	10 (CL3)	14	42	68	3
TS3	0 (CL0)	14	42	30	3
	1 (CL1)	14	42	30	3
	5 (CL2)	14	42	30	3

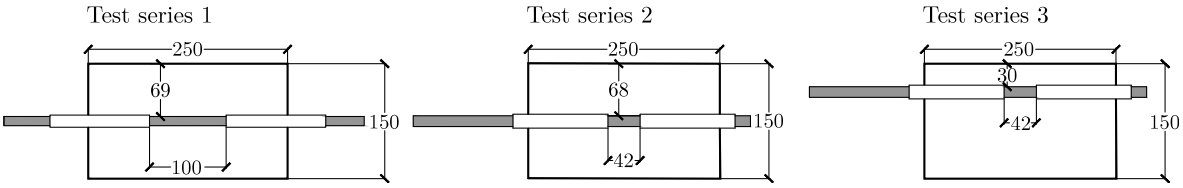

Fig. 1. Layout of the samples of (left) test series 1, (middle) test series 2, and (right) test series 3.

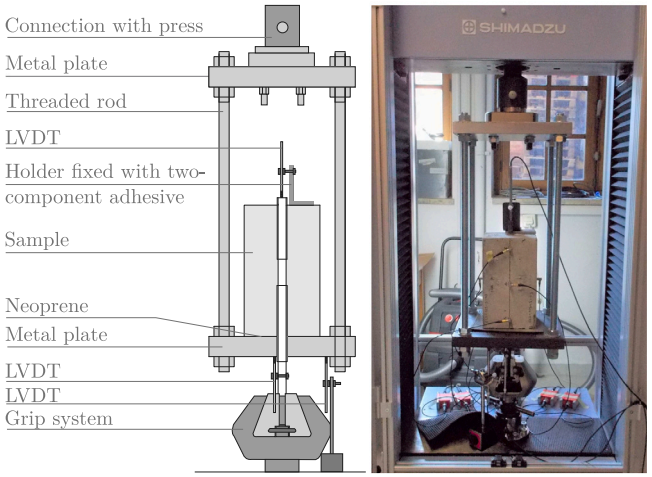

Fig. 2. Pull-out test setup with (left) schematic representation, and (right) picture.

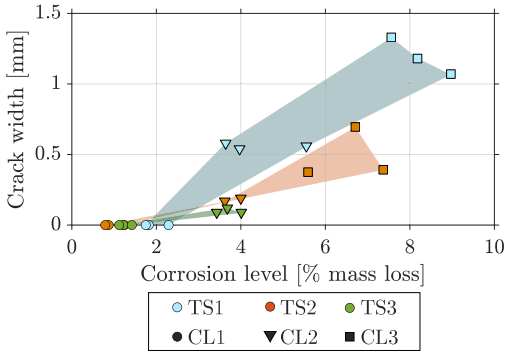

Fig. 3. Crack width versus corrosion level as obtained during the experiments for TS1, TS2, and TS3 with indication of the different corrosion levels CL1, CL2, and CL3 (see also Table 1).

for the entire test. A Linear Variable Differential Transformer (LVDT) was attached to the free rebar end to measure the slip.

After the pull-out tests, the actual corrosion level, expressed as a percentage of the mass loss, was determined by removing the rebars from the samples and cleaning them with Clark's solution according to ASTM G1-03 [21].

2.2. Summary of the experimental results

Fig. 3 shows the measured crack width versus corrosion level (CL) of each sample as obtained at the end of the corrosion experiments. This crack width is an average crack width as obtained from 9 (TS1) or 12 (TS2 and TS3) measurements at different locations along the concrete surface, using a crack meter. All cracked samples showed a longitudinal crack over the entire length of the sample (250 mm). Thus, the crack length was the same for each test series regardless of the bonded length and concrete cover.

The experimental results show that larger crack widths are found for TS1 which are the samples with the largest bond length and concrete cover thickness. For similar corrosion levels, smaller crack widths are found for TS2. The major difference between TS1 and TS2 is the shorter bond length being 100 mm for TS1 and 42 mm for TS2. From these results it seems that a shorter bond length leads to more confinement of the concrete in the uncorroded part and therefore a smaller crack width. The crack model should thus take into account a difference in confinement.

For TS3, only two corrosion levels were tested, CL1 and CL2, besides the reference samples. Compared to TS2, a slightly smaller crack width is obtained for TS3. The bond length is similar, but the concrete cover thickness is smaller in case of TS3. Although this difference in crack width is less significant, it is in agreement with data from corrosion tests in the literature [22].

Fig. 4 shows the bond stress versus slip for each test series as obtained during the experimental pull-out tests. The bond stress is calculated as the normal force divided by the surface area of the rebar embedded in the concrete, i.e. bonded length, and the slip as the displacement of the LVDT at the free end of the rebar (see Fig. 2). Note that the samples of CL1 of TS1 failed by rupture of the rebar and are therefore not shown. The results of TS2 show a marked increase of the bond strength for a low corrosion level (CL1) compared to the reference samples. It should be noted that this increase is higher than test series found in the literature which is probably caused by the large concrete

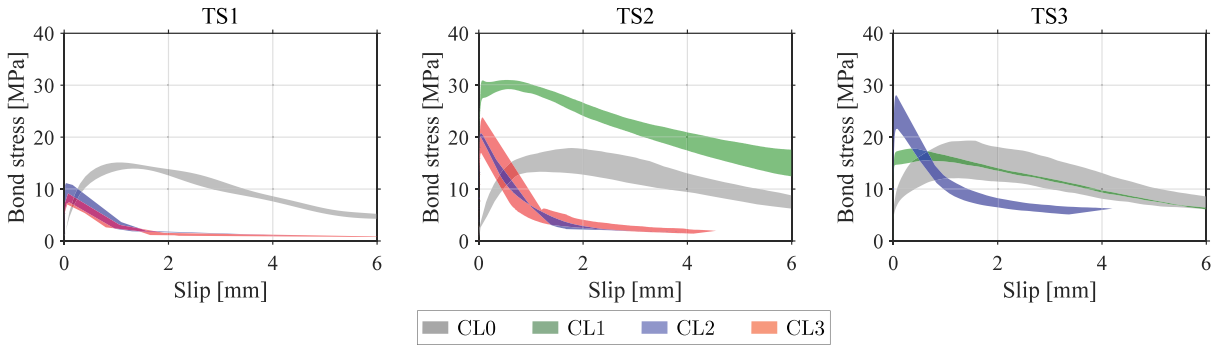

Fig. 4. Experimental bond–slip results with (left) TS1, (middle) TS2, and (right) TS3.

cover and unbonded length [8,20]. In all test series, an increase in stiffness is observed for the corroded samples.

For the lowest corrosion levels (CL0 and CL1), pull-out failure can be observed. For higher corrosion levels (CL2 and CL3), samples were cracked before testing due to corrosion, and splitting failure was observed. It will therefore be important that the bond model is able to capture not only corrosion effects on the bond strength and stiffness, but also this change in failure mechanism.

Finally, as the experimental results are scattered, numerical results should be obtained for an 'average' sample, assuming an average corrosion level of each sample type, instead of modelling a specific sample.

3. Overview of the modelling approach

The modelling approach consists of a 2D crack model and 3D bond model. Although simplifications are made, a proper representation of the corrosion process in the crack model is necessary to obtain adequate results. Usually, the expansion of corrosion products is modelled as shown in Fig. 5 (top). Part of the steel is consumed, V_{loss}, leading to a decrease of the original steel volume, V_0. Corrosion products occupy a greater volume than the steel that is consumed. Depending on the type of corrosion products, a different volumetric expansion coefficient, α_V, is valid. Values for α_V range between 2 and 6 [23,24]. The total volume of corrosion products, V_{corr}, can be written as α_V times V_{loss}. The final unconfined expansion, $V_{corr,eff}$, can be written as:

$$V_{corr,eff} = V_{corr} - V_{loss} = (\alpha_V - 1)V_{loss} \quad (1)$$

The corrosion process according to Eq. (1) can be implemented in an FE model using a thermal analogy in which the expansion of corrosion products is modelled by a thermal expansion of the rebar. However, it was noted in a preliminary study that in this simplified approach, the resulting bond strength is too high in comparison with the experimental data. Therefore, a corrosion-crack model is implemented in the current work, in which the flow of corrosion products into cracks, V_{flow}, is taken into account. It is experimentally observed that corrosion products migrate or diffuse in the cement matrix and corrosion-induced cracks [24,25]. This flow plays an important role in the release of the pressure build-up and resulting bond strength as was observed by several authors [17,26,27]. It is also reported in the literature that the flow of corrosion products in the corrosion accommodation region (CAR) has an important influence on reducing the stress build-up in the concrete [16,28]. Therefore, this mechanism is also taken into account by introducing V_{CAR}. Eq. (1) is therefore adapted to:

$$V_{corr,eff} = V_{corr} - V_{loss} - V_{CAR} - V_{flow} \quad (2)$$

This adaptation is visualised in Fig. 5 (bottom). Taking into account the CAR will lead to a shift in time, meaning that the pressure build-up is postponed. By including the flow of corrosion products into cracks, the effective expansion rate of rust will decrease over time.

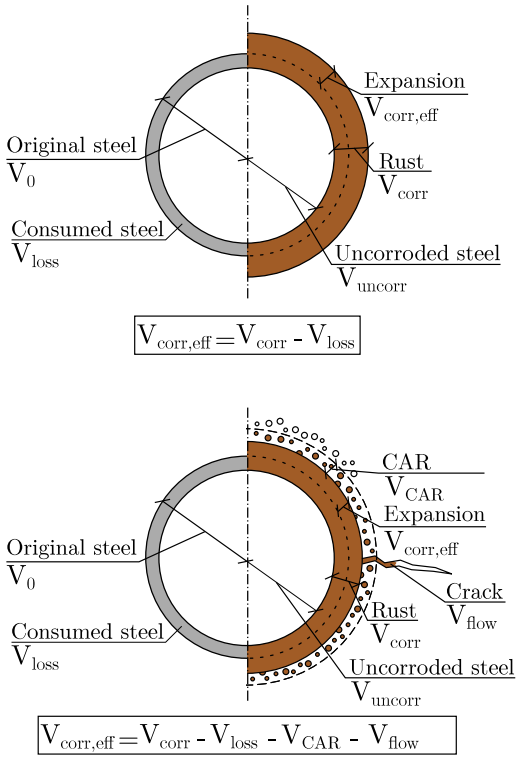

Fig. 5. Representation of the variables of the corrosion process: (top) original assumption (based on [14]), and (bottom) adapted approach followed in this paper.

Fig. 6 gives an overview of the two-phased modelling approach. The model consists of a 2D crack model according to the approach presented above, and a 3D bond model. The models are implemented using Matlab and the FE software Diana 10.5. The aim of the crack model is to calculate the correct expansion of corrosion products and crack width, which are input for the bond model. The output of the bond model is a bond–slip or $\tau - \delta$ relation which can be used for the modelling of the structural capacity of RC components. This last step is indicated by dashed lines in Fig. 6 as it is not within the scope of the current work.

4. Crack model implementation

The aim of the crack model is to obtain a value for the crack width and the expansion of the corrosion products, u_{corr}, which is based on the effective volume of corrosion products, $V_{corr,eff}$. Following Eq. (2), $V_{corr,eff}$ is determined by the total amount of generated corrosion products, V_{corr}, the volume of consumed steel, V_{loss}, the volume of the CAR,

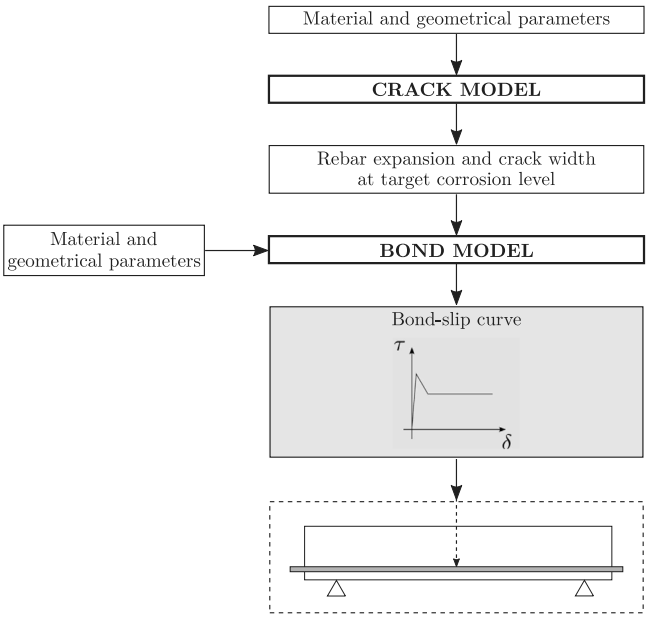

Fig. 6. Overview of the modelling approach.

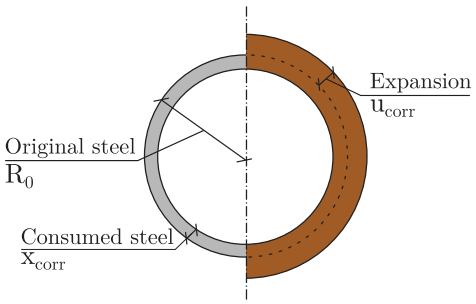

Fig. 7. Basic geometrical considerations to model uniform corrosion.

V_{CAR}, and the volume of corrosion products flowing in cracks, V_{flow}. The analysis is performed in time steps corresponding to an amount of corrosion days with a given corrosion rate. For each time step, $V_{corr,eff}$ is determined. In following subsections, these four parameters are discussed, and hereafter the implementation itself is described.

4.1. Volume of corrosion products, V_{corr}, and steel volume loss, V_{loss}

The 3D volumetric problem is translated to a radial expansion of the rebar (1D approach) [12,19]. The free expansion of corrosion products u_{corr} is determined from x_{corr}, the thickness of the consumed steel layer or corrosion penetration depth (Fig. 7). The percentage of steel mass loss or corrosion level (CL), can be written as the ratio between the consumed steel V_{loss} and the original amount of steel V_0:

$$CL = \frac{V_{loss}}{V_0} \cdot 100 = \frac{R_0^2 \pi L_{corr} - (R_0 - x_{corr})^2 \pi L_{corr}}{R_0^2 \pi L_{corr}} \cdot 100, \tag{3}$$

where R_0 is the initial radius and L_{corr} is the length of the corroding part of the rebar.

From Eq. (3), following expression for x_{corr} can be obtained:

$$x_{corr} = R_0 \cdot (1 - \sqrt{1 - \frac{CL}{100}}) \tag{4}$$

The volume of rust (V_{corr}) relative to the volume of consumed steel is determined by parameter α_V, which is the expansion coefficient of the corrosion products (Eq. (5)).

$$V_{corr} = \alpha_V V_{loss} \tag{5}$$

Based on Fig. 7, the volume of corrosion products can be written as:

$$V_{corr} = (R_0 + u_{corr})^2 \pi L_{corr} - (R_0 - x_{corr})^2 \pi L_{corr}, \tag{6}$$

where u_{corr} is the thickness of the unrestrained corrosion products.

Substituting Eq. (6) and the expression of V_{loss} from Eq. (3) in Eq. (5) gives following expression for u_{corr}:

$$u_{corr} = \sqrt{R_0^2 + (2R_0 x_{corr} - x_{corr}^2)(\alpha_V - 1)} - R_0 \tag{7}$$

Eq. (7) only takes into account V_{corr} and V_{loss}. This will be adapted in following subsections taking into account V_{CAR} and V_{flow} as well.

A linear rust production in function of exposure time based on Faraday's law is assumed. The type of corrosion product that is formed strongly depends on environmental conditions, e.g. oxygen availability and chloride content. Therefore, corrosion products in accelerated corrosion tests will be different from those occurring in natural conditions [29]. Several researchers reported on experimental tests in which the corrosion process is accelerated in a similar way. Fischer et al. [30] reported the presence of goethite (α-FeOOH, $\alpha_V = 2.92$), lepidocrocite (γ-FeOOH, $\alpha_V = 3.06$), and akaganeite (β-FeOOH, $\alpha_V = 3.48$) in their accelerated corrosion tests. Goethite and lepidocrocite were also found in the tests of Liu et al. [31]. Similar findings were obtained by Zhao et al. [32] and Shi and Ming [33]. Sola et al. [29] reported the presence of goethite in case of tests accelerated with 100 mV and akaganeite in case of 500 mV. For the current work, a combination of goethite and lepidocrocite is assumed, leading to an expansion coefficient α_V of 3.

4.2. Corrosion accommodation region, V_{CAR}

The internal stresses caused by the expansion of corrosion products will be reduced by the presence of a CAR as discussed by several researchers [16,28]. The CAR is a porous zone around the rebar which can be filled with corrosion products leading to a delay in the stress build-up in the concrete. First, the pores of an initial zone, CAR_0, will be filled with corrosion products. Second, when this initial zone is filled, tensile stresses will increase and micro-cracks will form. Due to these micro-cracks, additional pores can be filled which further delays the stress build-up. The maximum size of this additional zone is called CAR_{max}. When CAR_{max} is filled, tensile stresses in the concrete will increase due to the formation of additional corrosion products resulting in the formation of macro-cracks.

Usually the thickness of this porous zone is used as a fitting parameter. Experimentally obtained values are therefore scarce in the literature. Values between 0.002 and 0.12 mm were reported [25,28], however, the CAR was determined by cutting and sawing of corroded samples which can possibly remove corrosion products. Michel et al. [34] obtained values ranging between 0.11 and 0.45 mm based on 2D micro-CT measurements. It was also reported that the extent of the CAR is influenced by the current density and concrete composition, such as water/cement ratio [34]. In the current study, the definition and calculation of CAR is based on CAR_{max} as presented in Michel et al. [16]. The extent of CAR_{max} is obtained from 3D CT-imaging [35]. For each of the CT-images of corroded, but uncracked samples, corrosion products are segmented based on their density value. The maximum CAR is determined as the maximum difference between the radius of the zone with corrosion products and the original radius of the rebar. Note that there is already deformation of the concrete and that this small deformation is not taken into account in this simplified approach. Moreover, the calculation of the CAR depends on the resolution of the X-ray scans, which was 18 μm. An averaged value equal to 0.73 mm is found. This value is higher than currently applied values in the literature which can be caused by a

different composition and compaction degree [26]. Also the presence of interfacial voids which were not observed in the 2D setup of Michel et al. [34] will influence the results. These voids are clearly visualised by the current 3D setup. Interfacial voids were also observed by Rossi et al. [36] who performed 3D micro-CT scanning on naturally corroded samples.

The CAR volume, V_{CAR}, only contains pores that can be filled with corrosion products and can therefore be calculated as [34]:

$$V_{CAR} = \phi V_{CM}, \tag{8}$$

with ϕ the porosity of the concrete matrix and V_{CM} the volume of the concrete matrix between the rebar and CAR_{max}. V_{CM} can be calculated as:

$$V_{CM} = \pi L_{corr}(R_0 + CAR_{max})^2 - \pi L_{corr} R_0^2, \tag{9}$$

where L_{corr} is the length of the corroding part of the rebar and R_0 the original radius of the rebar.

In this paper, the porosity is determined experimentally on three samples according to NBN B 24-210 [37]. The average porosity is found to be 11.01% (standard deviation 0.37%).

4.3. Flow of corrosion products in cracks, V_{flow}

The amount of corrosion products that flow in the cracks is still under debate and depends on the concrete cover depth, crack size and distribution, corrosion rate, and other parameters of the corrosion process. In modelling approaches, this parameter is usually calibrated on experimental results, or a detailed diffusion model can be applied [38]. The latter approach leads to additional parameters which can in turn not all be determined experimentally. This extensive approach was therefore not followed in the current paper. In this paper, the final crack width due to corrosion before pull-out testing (e.g. at a certain moment of condition assessment) is of interest rather than the evolution of the cracking process over time. Therefore, a more pragmatic approach was sought. A similar approach as Andrade and Anaya [39] was followed, namely assuming a percentage of the corrosion products to fill the cracks and therefore releasing part of the internal pressure build-up. The implementation is described below.

As V_{flow} represents the flow of corrosion products into the corrosion cracks being formed (V_{crack}), a step-wise process of corrosion-pressure build-up, cracking, and rust flow occurs. Therefore, the analysis is performed in time steps. Each time step i represents a number of corrosion days at a given corrosion rate. The developed crack model allows to calculate in a step-wise manner the volume of corrosion products flowing in the cracks generated due to the corrosion process, $V_{flow,i}$, which will reduce the pressure build-up in the concrete. After each time step, the total volumetric strain is obtained. The total volumetric strain of a 2D element k is equal to:

$$\epsilon_{vol,k} = \epsilon_{1,k} + \epsilon_{2,k} = \frac{\Delta V_k}{V_{0,k}} \tag{10}$$

with $\epsilon_{1,k}$ and $\epsilon_{2,k}$ the in-plane principal strains, ΔV_k the volume change of element k, and $V_{0,k}$ the original volume of element k. For smeared crack models, Diana assumes a default crack band width (CBW) which is $\sqrt{A_0}$ for 2D elements. It is assumed that the volume change of all elements, i.e. the summation of the ΔV_k's of each element, is caused by the expansion of the rebar and by the formation of corrosion-induced cracks. Therefore, the crack volume at time step i, $V_{crack,i}$, is equal to:

$$V_{crack,i} = \sum_{k=1}^{n} \epsilon_{vol,k} \cdot V_{0,k} - \sum_{l=1}^{m} \epsilon_{vol,l} \cdot V_{0,l}, \tag{11}$$

with n all integration points of all the elements of the sample, and m all integration points belonging to the elements of the rebar.

So far, no reliable experimental data have been reported to quantify the amount of rust flowing in corrosion cracks. Many models assume that the entire crack is filled with corrosion products [26,27]. From visual observation of the split samples after the pull-out tests (Fig. 8) and from first modelling attempts, it is found that assuming a complete filling of the cracks is an overestimation, certainly for higher corrosion levels. A sensitivity study was performed by Andrade and Anaya [39]. Here, a flow of 20% of the formed corrosion products was found for large cover-to-diameter ratios. For smaller ratios, a higher percentage of corrosion products was considered to flow in the cracks.

Fig. 8. Picture of a split sample after a pull-out test.

Current work assumes that a small percentage Φ_1 of the new crack volume, $\Delta V_{crack,i}$, is filled with corrosion products when having small cracks as there will be more space to accommodate the corrosion products compared to the uncracked situation [16]. When the cracks become larger and reach the surface, it should be considered that the amount of corrosion products flowing in the cracks cannot become larger than the amount of produced corrosion products. If this would be the case, it is assumed that a percentage Φ_2 of the produced corrosion products $\Delta V_{corr,i}$ flow in the crack, following the findings of Andrade and Anaya [39]. In both cases, the amount of corrosion products flowing in the crack is added to the volume of corrosion products inside the crack from the previous time step, $V_{flow,i-1}$. To summarise, the new crack volume that is filled with corrosion products, $V_{flow,i}$, is calculated as:

$$V_{flow,i} = V_{flow,i-1} + \Delta V_{flow,i} \tag{12}$$

with

$$\Delta V_{flow,i} = \begin{cases} \Phi_1 \Delta V_{crack,i}, & \Phi_1 \Delta V_{crack,i} < \Delta V_{corr,i} \\ \Phi_2 \Delta V_{corr,i}, & \Phi_1 \Delta V_{crack,i} \geq \Delta V_{corr,i} \end{cases} \tag{13}$$

A value of 10% was assumed for Φ_1. A value of 20% was used for Φ_2 for TS1 and TS2 as these have large concrete covers. For smaller covers, more corrosion products will flow in the cracks [39]. Therefore, Φ_2 was adapted to 50% for TS3.

The formula for u_{corr} as defined in Eq. (7) can now be adapted including V_{CAR} and V_{flow}:

$$u_{corr} = \sqrt{R_0^2 + \frac{V_{corr,eff}}{\pi L_{corr}}} - R_0 \tag{14}$$

with $V_{corr,eff} = V_{corr} - V_{loss} - V_{CAR} - V_{flow}$.

4.4. Implementation of the crack model

To limit the computational time, a 2D plane strain model was used, similar to the approach used by Thybo et al. [40]. A cross-section of 150 mm × 150 mm is modelled in Diana. The units are set in mm meaning that it is assumed that the section has a thickness of 1 mm. To calculate the volumes as mentioned in the previous sections, the output should be multiplied with the bonded length. The models are shown in Fig. 9. Plane strain elements with a quadratic interpolation function were used. This allows to model a linearly varying stress and strain field in the element. As a uniform expansion was assumed, the mesh was made asymmetric by adding a small line element in order to

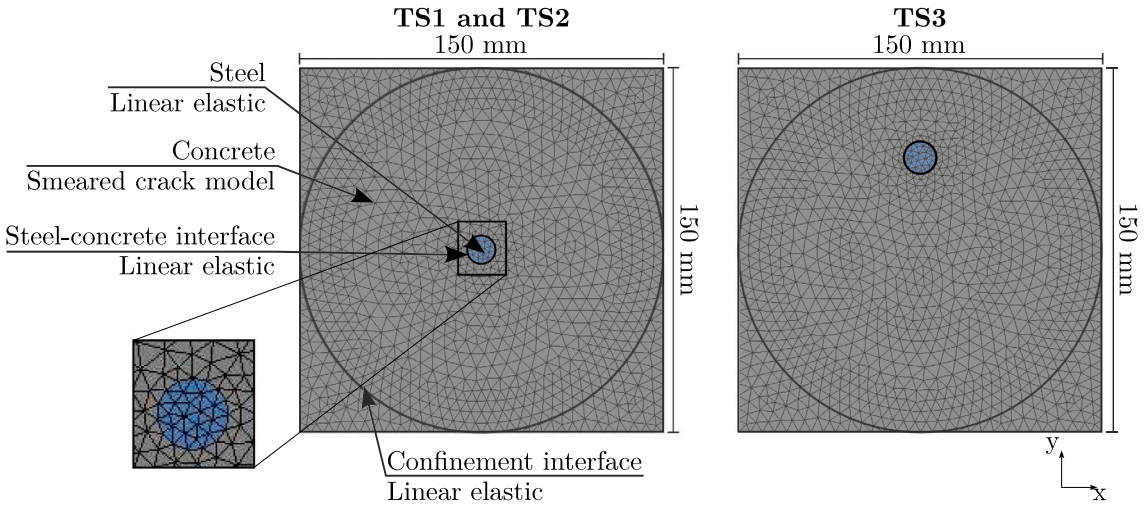

Fig. 9. Crack model with indication of different materials and elements with (left) the implementation for TS1 and TS2 with a centrically positioned rebar and (right) for TS3 with an eccentrical rebar and reduced cover.

obtain one main crack in case of TS1 and TS2. As the concrete cover is smaller for TS3, this was not required as the crack would preferentially grow in the direction of the smallest concrete cover. The properties of the different materials, such as steel, concrete, and the steel-concrete interface, as well as the implementation of a different confinement, are described in following subsections.

4.4.1. Steel properties

The Young's modulus of corrosion products (E_{rust}) is smaller than the Young's modulus of steel (E_s). Values between 2 and 100 GPa are found in the literature for the Young's modulus of corrosion products [41]. In most papers, linear elastic behaviour is assumed [23,42]. Michel et al. [43] proposed a value of 2 GPa. Toongoethong and Maekawa [44] and Savija et al. [26] applied a value of 7 GPa. In contrast, Lundgren [14] proposed a non-linear behaviour with an important permanent strain. This was experimentally confirmed by Ouglova et al. [45] to be a reasonable approach.

In the current work, a value of 2 GPa is assumed. It was observed that this value has a limited effect on the modelled results when ranging between 1 and 14 GPa, which is line with the previously described values from other researchers. Molina et al. [42] also observed a limited effect for values in the same order of magnitude.

As the Young's modulus of corrosion products is 100 times smaller than the Young's modulus of steel, the Young's modulus of the rebar needs to be adapted in every time step. Following Toongoethong and Maekawa [44], an equivalent Young's modulus, E_{eq}, is assigned to the rebar, incorporating the amount of steel and corrosion products:

$$E_{eq} = \frac{R_0^2}{\frac{(R_0 - x_{corr})^2}{E_s} + \frac{[(R_0 + u_{corr})^2 - (R_0 - x_{corr})^2]}{E_{rust}}} \tag{15}$$

The steel is assumed to be linear elastic. The properties are summarised in Table 2. The expansion of corrosion products is modelled using a thermal analogy which means that a thermal load is applied to the reinforcement [46]. The thermal expansion of the original radius R_0 leads to a new expanded radius R_{exp}. The radius increase ΔR is the product of a linear thermal expansion coefficient α_D with the temperature increase ΔT and the initial radius R_0:

$$R_{exp} = R_0 + \Delta R = R_0 + \alpha_D R_0 \Delta T, \tag{16}$$

where R_{exp} is the new rebar radius at a certain corrosion level, α_D is the linear thermal expansion coefficient, and ΔT is the temperature change. It is in Diana not possible to vary α_D for each time step and consider all previous values at the same time. It is therefore decided to keep α_D constant and to vary ΔT, following Michel et al. [46]. A thermal expansion coefficient equal to 1 is assigned to the material properties of the rebar. ΔR is equal to u_{corr} in case of uniform corrosion, as defined in previous sections. ΔT will hence be equal to:

$$\Delta T = \frac{u_{corr}}{R_0} \tag{17}$$

The evolution of ΔT in time is implemented in Diana by attributing ambient time dependencies to the rebar at different time steps to mimic the expansion due to corrosion. In the current work, uniform corrosion around the rebar circumference is applied, however, an extension towards non-uniform corrosion is possible by assuming non-uniform ΔT values.

Table 2
Input parameters steel.

	Parameter	Value	Dimension
Young's modulus steel	E_s	210	GPa
Young's modulus rust	E_{rust}	2	GPa
Temperature change	ΔT	according to Eq. (17)	°C
Equivalent Young's modulus	E_{eq}	according to Eq. (15)	GPa

Table 3
Input parameters concrete.

	Parameter	Value	Dimension
Young's modulus	E_c	34	GPa
Poisson's ratio	ν_c	0.2	–
Mean concrete compressive strength	f_{cm}	43	MPa
Mean tensile strength	f_{ctm}	3.2	MPa
Mode-I tensile fracture energy	G_f	0.14	N/mm

4.4.2. Concrete properties

A smeared crack approach is used to model concrete cracking, using a total strain fixed crack model. Material properties are obtained from tests performed on cubes and prisms [8,20]. The assigned concrete class is C35/45. Material properties are summarised in Table 3. The compressive behaviour is assumed to be elastic, the tensile curve exponential and the shear retention function constant.

4.4.3. Steel-concrete interface properties

Interface elements are used between the rebar and concrete to represent the connection between the two materials. These interface

Table 4
Overview of the normal stiffness values applied for the confinement ring.

Test series (TS)	Bond length [mm]	Interface stiffness [N/mm^3]
TS1	100	5
TS2	42	100
TS3	42	100

elements describe the relation between the traction t and relative displacement Δu across the interface and have zero thickness [47]:

$$\begin{bmatrix} t_n \\ t_s \\ t_r \end{bmatrix} = \begin{bmatrix} D_n & 0 & 0 \\ 0 & D_s & 0 \\ 0 & 0 & D_r \end{bmatrix} \begin{bmatrix} \Delta u_n \\ \Delta u_s \\ \Delta u_r \end{bmatrix} \tag{18}$$

where t_n is the normal traction perpendicular to the interface, t_s and t_r are the shear tractions tangential to the interface, D_n is the interface elastic normal stiffness modulus [N/mm^3], D_s and D_r are the interface elastic shear stiffness moduli [N/mm^3], Δu_n is the normal displacement, Δu_s is the slip, and Δu_r is the rotation of the rebar. In case of a 2D model, only t_n and t_s are required, meaning that t_r, D_r, and Δu_r are omitted from Eq. (18). Values of 1000 and 100 N/mm^3 respectively for D_n and D_s are used. These stiffness values are in line with what is found in the literature [11,15].

4.4.4. Confinement

Besides the variation in cover thickness, which is explicitly modelled, one of the main differences between the test series, is the difference in bonded length, which is equal to the corroding length. As the total length of the samples is kept the same for all test series, this will have an effect on the uncorroding length and hence the confinement of the sample as was discussed in Section 2.2. In previous research, it was found that this is an important parameter to take into account [48–50].

In this paper, the effect of passive confinement due to the surrounding concrete is implemented by adding a confinement ring which is a circular 2D interface with a normal stiffness D_n. This normal stiffness is adapted based on the ratio between the corroding or bonded length and the total length of the sample. Therefore, a difference between TS1 (L_{bond} = 100 mm) and TS2 and TS3 (L_{bond} = 42 mm) can be accounted for.

As this is a novel approach and no literature values could be found, the value of D_n is determined based on calibration with the experimental results. By minimising the sum of the squares of the residuals, which is in this case the difference between the experimentally observed crack width and the modelled crack width, the interface stiffness is determined. The values are summarised in Table 4 and are applied on all corrosion levels.

5. Bond model implementation

For the bond model, a 3D symmetric model is implemented that makes use of the symmetry of the pull-out samples along a vertical plane, see Fig. 10. The models consist of solid elements with a quadratic interpolation function for both the concrete and reinforcement. Interface elements are used between the rebar and concrete to represent the bonded or unbonded connection between the two materials.

5.1. Steel properties

The corroded rebar is modelled as a linear elastic material. The same steel material properties are used as in the crack model (see Table 2). From the output of the crack model the equivalent thermal load ΔT is extracted for the desired corrosion level and imposed on the corroded and bonded part of the steel rebar in the bond model.

5.2. Concrete properties

Similarly to the crack model, a total strain fixed crack model is assigned to the concrete material. The same concrete class is assumed (see properties in Table 3). A surface interface is added in all samples representing a discrete crack. The tensile strength of the interface is assumed to be 3.2 N/mm^2 when the sample is not cracked at the end of the corrosion process and 0 N/mm^2 when the sample is cracked. The tensile strength of the uncracked interface is equal to the concrete tensile strength. This discrete crack is added at the position where the main crack is observed during the experiments, see Fig. 10. The combination of discrete and smeared cracking allows to only model half of the sample reducing the computational time and to correctly represent the corrosion crack that is obtained by the crack model.

5.3. Interface properties

Similar to the crack model, interface elements are used between the rebar and concrete to represent the connection between the two materials. The same value for D_n as in the crack model, 1000 N/mm^3, is used. D_s is set equal to 205 N/mm^3, which is the same value as in Lundgren et al. [51]. D_r is taken equal to D_s.

A Coulomb friction model is used at the interface between the corroding, bonded length of the rebar and the concrete. This model allows irreversible relative displacements to occur when the two faces of the interface element are in contact [47]. Therefore, it is assumed that the relative displacements, $\boldsymbol{\Delta u}$, can be decomposed in an elastic (reversible), $\boldsymbol{\Delta u^e}$, and plastic (irreversible), $\boldsymbol{\Delta u^p}$, part:

$$\boldsymbol{\Delta u} = \boldsymbol{\Delta u^e} + \boldsymbol{\Delta u^p} \tag{19}$$

The Coulomb friction model for the corroded rebar interface is defined as

$$t_s(s, CL) = c(s) + \tan(\phi(s, CL)) t_n(s), \tag{20}$$

with t_s the shear traction, c the cohesion, ϕ the friction angle, and t_n the normal traction. The shear traction and friction angle vary with increasing slip and corrosion level. The cohesion and normal traction vary with increasing slip.

For non-corroded samples, values between 0.5 and 1.5 N/mm^2 are proposed by the fib Model Code for the cohesion [3]. In this paper, the cohesion was set at 0.75 N/mm^2, following bond tests on samples with smooth rebars [20]. However, note that the effect of cohesion is limited in case of ribbed rebars.

The friction angle can be written in terms of the coefficient of friction μ:

$$\phi = \tan^{-1}(\mu), \tag{21}$$

The value of the friction angle at zero slip, i.e. initial friction angle, was fitted based on the uncorroded samples of TS1 resulting in 63° or μ_0 equal to 2. To account for a correct representation of the post-peak behaviour, the decrease of the coefficient of friction in function of the slip is based on the Combined Cracking-Shearing-Crushing model in Diana to obtain an exponential decay [47]:

$$\mu(s) = \mu_{res} + (\mu_0 - \mu_{res}) e^{\frac{-c_0}{G_f^{II}} s}, \tag{22}$$

with μ_0 and μ_{res} the initial and residual coefficient of friction respectively, c_0 the initial cohesion, and G_f^{II} the shear-slip fracture energy. The parameters μ_0 and μ_{res} are set to 2 and 0.05 respectively, based on the post-peak behaviour of the uncorroded samples (CL0) of TS1. The initial cohesion c_0 is equal to 0.75 N/mm^2 as mentioned before and G_f^{II} is equal to 1.049 N/mm following Bazant et al. [52].

In addition, the relation of the friction angle versus slip depends on the corrosion level. For a certain corrosion level, $\phi(s)$ as determined in case of CL0 (i.e. $\phi(s,0)$) is adapted by a factor η. This factor is based on the fib Model Code [3] giving a rough estimation of the

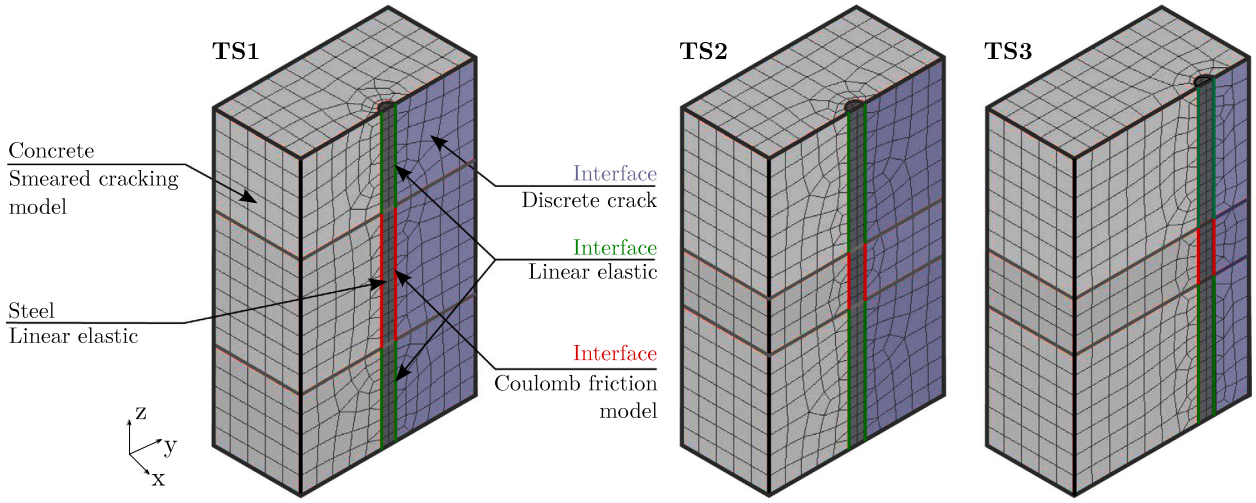

Fig. 10. Bond model with indication of different materials and elements with implementation for the sample layout in (left) TS1, (middle) TS2, and (right) TS3.

Table 5
Magnitude of the reduction of the bond strength depending on the corrosion penetration and equivalent surface crack width, based on [3].

Corrosion penetration [mm]	Equivalent surface crack [mm]	Residual capacity (%)
0.05	0.2–0.4	50–70
0.1	0.4–0.8	40–50
0.25	1.0–2.0	25–40

residual capacity in function of the corrosion penetration depth x_{corr} and equivalent crack width as shown in Table 5. As the residual bond strength in the model is mainly determined by the coefficient of friction, the reduction of this parameter is based on the values from the Model Code rather than fitting the results with the experiments.

For the current experiments, it is observed that the crack widths for the obtained corrosion levels (or corrosion penetration depth following Eq. (4)) are smaller than the equivalent surface crack widths as described by the fib Model Code [3]. The crack width depends on a number of parameters, including cover depth and rebar diameter, and it is not clear which assumptions are made in the Model Code. In the current paper, the corrosion penetration depth instead of the crack width is used to determine the percentage values for the residual capacity. For the average corrosion level of each test series, the factor η is calculated by linear interpolation between the average values of the residual capacity as described in Table 5.

Moreover, the Model Code does not take into account the increase in bond strength for low corrosion levels which is clearly observed in the experimental results. For TS1, the samples of CL1 failed by rupture of the rebar, so no experimental values were obtained. For TS2, an increase of 100% in bond strength was observed, whereas for TS3, only an increase of 25% was observed. The large difference between TS2 and TS3 can probably be attributed to a difference in cover thickness [20]. To account for the bond strength increase for CL1, instead of applying a decrease of the friction angle depending on the corrosion level (or corrosion penetration depth) as proposed by the fib Model Code, the samples of CL1 will be modelled by assuming the same friction angle as for CL0.

To summarise, the friction angle which depends on the slip and corrosion level is calculated by Eq. (23). The values for the reduction factor η for each corrosion level and test series are shown in Table 6. Fig. 11 shows the relation of the friction angle versus slip for different corrosion levels of TS2. Curves for the other test series were determined similarly.

$$\phi(s, CL) = \phi(s, 0) - \phi(0, 0)\left[1 - \frac{\eta(CL)}{100}\right] \tag{23}$$

Table 6
Factor applied on the friction angle depending on the corrosion level.

Corrosion level	Factor η [%]		
	TS1	TS2	TS3
CL0	100	100	100
CL1	–	100	100
CL2	42	42	48
CL3	32	34	–

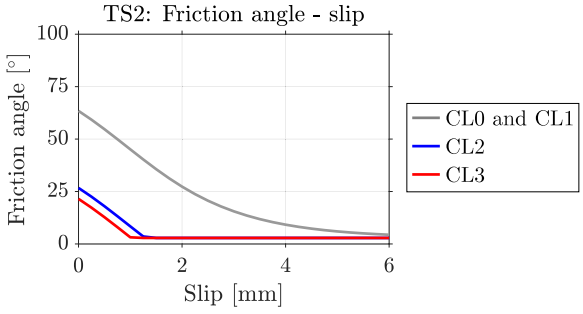

Fig. 11. Friction angle versus slip for different corrosion levels of TS2.

with $\phi(s, 0)$ the friction angle depending on the slip for corrosion level CL0 (combining Eqs. (21) and (22)), $\phi(0, 0)$ the friction angle at 0 mm slip of CL0, and $\eta(CL)$ a reduction factor depending on the corrosion level in % (Table 6).

5.4. Analysis procedure

A Newton–Raphson iteration scheme is used with a force convergence criterion. The analysis is performed in subsequent time steps. The thermal expansion of the rebar, mimicking corrosion, is applied in the first time step. Hereafter, a pre-described displacement in the global z-direction is applied to the nodes at the bottom of the steel rebar to simulate a pull-out test. The maximum displacement of 10 mm is reached in 2000 s. Therefore, the loading speed is the same as during the experimental pull-out tests: 0.3 mm/min.

6. Results and discussion

In this section, the simulation results of the developed two-phased numerical model are presented and compared with the experimental results. Firstly, the intermediate results of the crack model are discussed

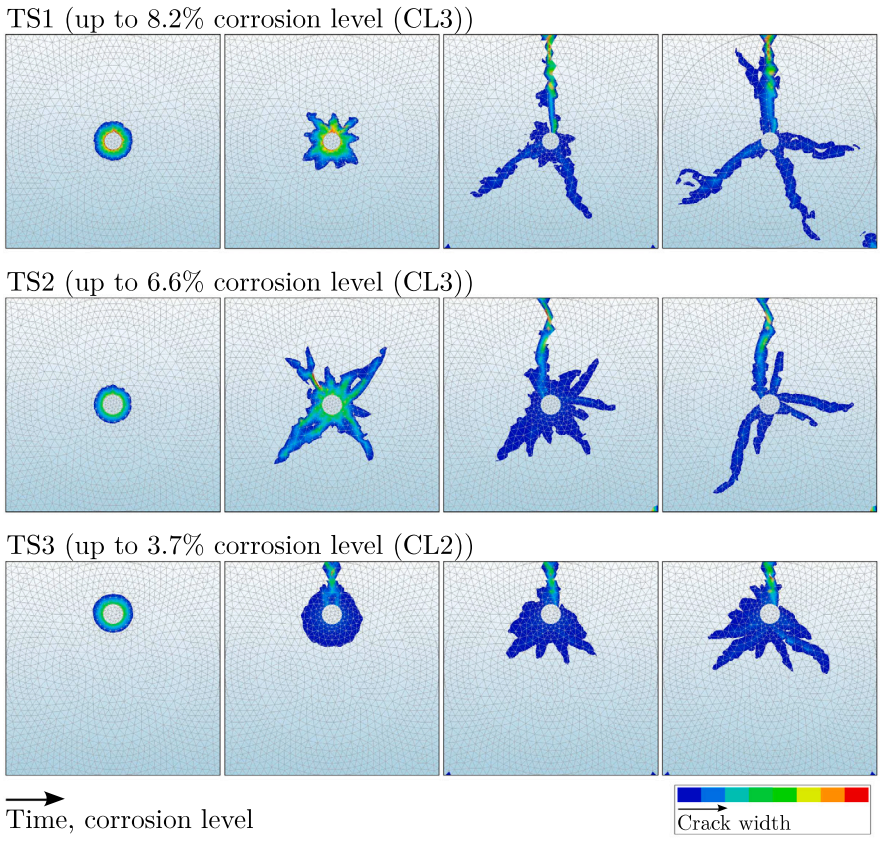

Fig. 12. Evolution of the crack pattern over time or corrosion level as obtained by the crack model for (top) TS1, (middle) TS2, and (bottom) TS3.

in terms of crack patterns and crack width evolution. From this first phase, the thickness of the corrosion expansion layer u_{corr} is deduced at a target corrosion level according to Eq. (14) and transferred into an equivalent temperature gradient ΔT following Eq. (17). Secondly, the bond model is applied with the obtained ΔT as input, and the resulting bond–slip relations are compared with experimental data.

6.1. Results crack model

Fig. 12 shows the evolution of the corrosion-induced crack pattern for each test series. Note again that average, representative corrosion levels and model parameters are used for each test series instead of a specific sample. For TS1 and TS2, the corrosion level in Fig. 12 increases up to CL3. For TS3, the corrosion-induced cracking up to CL2 is visualised. As expected, cracking starts internally in the vicinity of the rebar. The cracks grow towards the surface. For each test series, one main crack is formed as observed during the experiments. In case of a large concrete cover (TS1 and TS2), also additional cracks are formed. However, they do not reach the surface. It can be concluded that the crack model is able to correctly model the crack formation over time for the different test series.

Next, the width of the simulated main cracks is compared to the surface cracks measured during the experimental corrosion tests. As a smeared crack model is used, different approaches can be applied to obtain the crack width. In this paper, the modelled crack widths are calculated from the resulting strain fields using a virtual strain gauge, by analogy with a DEMEC mechanical strain gauge. The displacement in the horizontal X-direction of the two extreme surface nodes on the face of the main crack is used to obtain the crack width. This approach is chosen as it allows to determine the modelled crack width in the same way for each sample, and results can be compared to the experimental crack widths that were measured with a crack meter [8].

Table 7
Overview of the modelling results of the crack model.

Test series	Corrosion level	Average crack width (st. dev.) experiment [mm]	Crack width crack model [mm]
TS1	CL0	–	–
	CL2	0.57 (0.01)	0.57
	CL3	1.19 (0.11)	1.22
TS2	CL0	–	–
	CL1	–	–
	CL2	0.18 (0.01)	0.17
	CL3	0.49 (0.15)	0.40
TS3	CL0	–	–
	CL1	–	–
	CL2	0.10 (0.01)	0.11

Fig. 13 shows the experimental and numerical results of the final crack width versus corrosion level for each test series. It can be seen that the results of the crack model are in good agreement with the experimental data for all test series. Modelling an average sample rather than a specific sample allows to obtain adequate results lying within the experimental scatter. For all test series, CL1 did not result in surface cracks, which is also correctly captured by the crack model. The model can hence give a good indication of the average crack width that can be expected for a certain sample layout and corrosion level.

Table 7 gives a quantitative overview of the obtained results. For TS2 CL3, a larger difference between the experimental average crack width and modelled crack width can be seen. However, the experiments also showed a larger standard deviation for this corrosion level with one result being significantly larger than the other two. Nonetheless, the obtained modelled value lies within the experimental scatter and is a good representation of the crack width at this corrosion level.

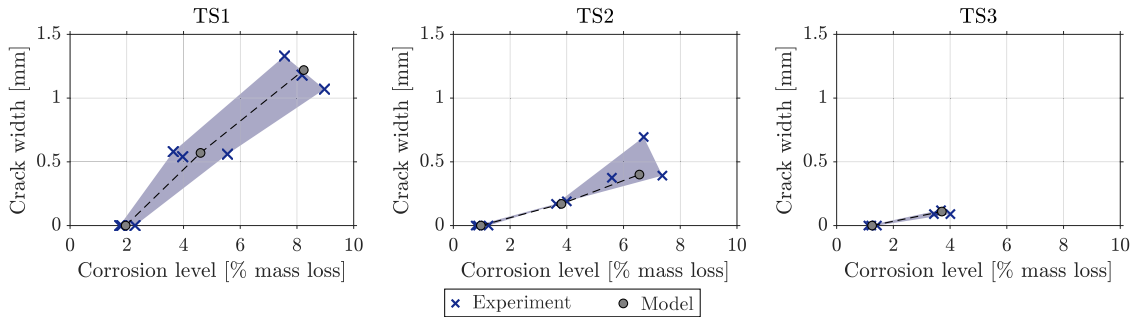

Fig. 13. Experimental and numerical results of the crack width versus corrosion level with (left) TS1, (middle) TS2, and (right) TS3.

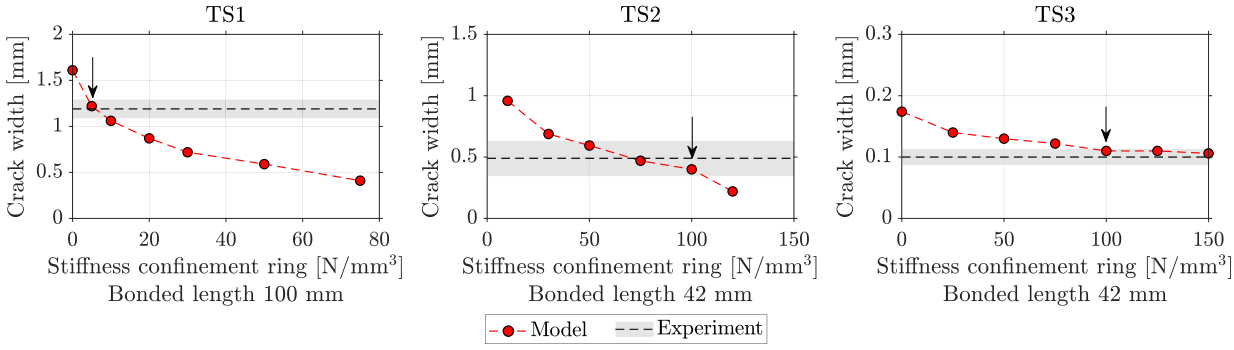

Fig. 14. Effect of different values of the stiffness of the confinement ring for (left) TS1, (middle) TS2, and (right) TS3, with indication of the average experimental results and scatter (dotted line and grey area) and chosen value in the model (arrow).

It can be anticipated that the results can be sensitive to the chosen values of the different model parameters. It was already mentioned before that a reasonable value of many parameters, such as the volumetric expansion coefficient of rust α_V, the Young's modulus of rust, E_{rust}, and the extent of the CAR, CAR_{max}, is chosen based on experimental data or obtained from the literature. It is important to note that certain parameters are related and without dedicated measurements (which are not always feasible), a different parameter set may lead to similar results. For example, the high stiffness of the corrosion products and large value for the CAR give a good result in terms of crack width using the current parameter set. With a smaller CAR, a smaller stiffness of the corrosion products, a higher percentage of corrosion products being transported through the cracks, or a smaller confinement would be required. A coupled sensitivity study is outside the scope of the current paper. However, the influence of the amount of corrosion products flowing is the cracks and the stiffness of the confinement ring are studied in more detail.

The effect of the stiffness of the confinement ring is shown in Fig. 14. Of course, the lower the stiffness value, the larger the crack width and vice versa. The chosen values, which are indicated by the arrow, gave best results considering the experimental scatter. Note that based on the results of TS2, a value around 75 N/mm^3 would result in a better fit. However, a value of 100 N/mm^3 was chosen for TS2 and TS3 as this gave best results for both test series. This is reasonable as for the three samples of TS2-CL3, one sample showed a significantly larger crack width compared to the other two samples (Fig. 13 and Table 7).

The effect of the flow of corrosion products in the crack is shown in Fig. 15. The results show a linear decrease of the crack width with increasing amount of corrosion products that flow in the crack. For TS2, no flow, i.e. 0%, would give a better result. However, a value of 20% was chosen for both TS1 and TS2 as these test series have the same concrete cover.

6.2. Results bond model

The results from the crack model are used as an input for the bond model of which the results are discussed for each test series in terms of the bond–slip relation and failure mode. Fig. 16 and Table 8 show the bond–slip relation for each test series and the quantitative values of the maximum force respectively.

For TS1, the results are in good agreement with the experimentally observed bond–slip relation. The failure mechanism is correctly obtained by the bond model. Pull-out failure can be seen for CL0, and splitting failure for CL2 and CL3. The increase of the stiffness is correctly represented as well by the bond model. The expansion of corrosion products first causes an increase of the normal traction t_n in the Coulomb friction model. When the pull-out force is simulated afterwards, the shear traction t_s increases until the yield surface is reached. By the friction angle-slip relation that is implemented based on the fib Model Code (Fig. 11), resulting in a lower value of the initial friction angle compared to CL0 and a sharp decrease with increasing slip, the reduction of the bond stress and the failure mode are correctly obtained.

Similar findings can be observed for TS2. Here, a higher value of the bond strength can be seen for CL2 and CL3 compared to CL0, both experimentally as by the model. Although the corrosion levels of CL2 and CL3 of TS2 are lower than the ones found for TS1, the corrosion penetration x_{corr} will almost have the same value as the rebar diameter is larger in case of TS2 (see Eq. (4)). This will result in a similar increase of the normal traction and decrease of the friction angle. However, as the bond length is different, a higher bond strength is eventually found in case of TS2.

As discussed before, the fib Model Code only assumes a decrease of the residual capacity with increasing corrosion penetration. However, for low corrosion levels, an increase of the bond strength can experimentally be observed. In the current approach, the model for CL1 makes use of the same friction angle-slip relation as CL0. Therefore, the only difference is the increase of the normal traction when corrosion is

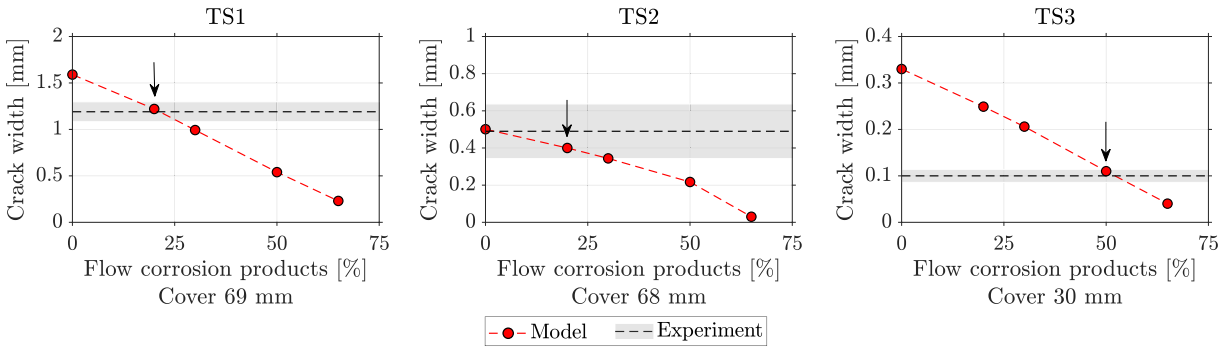

Fig. 15. Effect of different values of the flow of corrosion products into cracks for (left) TS1, (middle) TS2, and (right) TS3, with indication of the average experimental results and scatter (dotted line and grey area) and chosen value in the model (arrow).

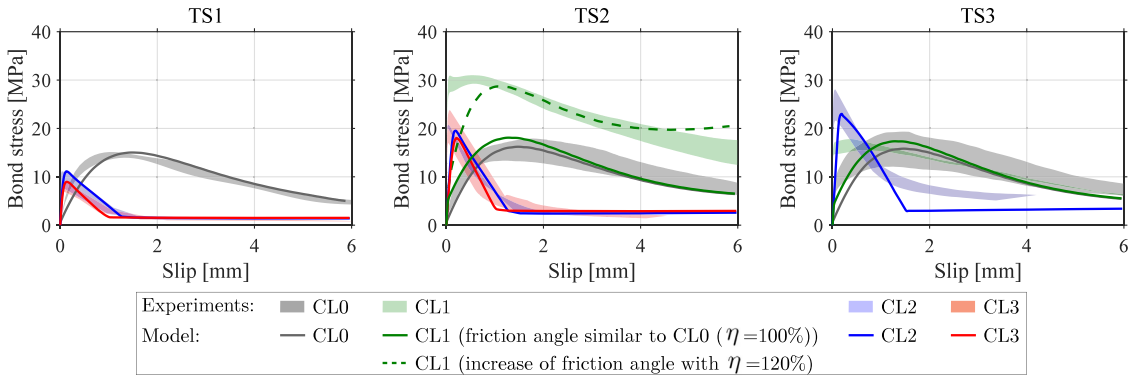

Fig. 16. Experimental and numerical results of the bond stress versus slip for various corrosion levels with (left) TS1, (middle) TS2, and (right) TS3.

simulated by the bond model. In case of TS2, it can be observed that the increase in bond strength is too small when only considering the expansion due to corrosion. As mentioned before, this increase is higher compared to values from the literature. This is probably caused by the large concrete cover and unbonded length. When a factor η of 120% is used, a better fit of the bond strength can be obtained as shown by the dotted line. In the crack model (2D), the confinement is incorporated by the confinement ring, which is a good approach to incorporate information of the confinement of the 3D sample without extensive computational effort. In the bond model (3D), the confinement is determined by the material properties of the concrete and steel-concrete interface. Therefore, an increase of the friction angle may be required. For TS3, the initial assumption of η equal to 100% gives a good result in terms of bond strength. In case of the small concrete cover, it seems that the increase in bond strength is less pronounced compared to larger concrete covers. More research is therefore required to correctly implement the possible increase in bond strength for uncracked samples with a low corrosion level.

Other results of TS3 follow the same trends as found for TS1 and TS2. For CL2, both the increase in bond strength and failure mode are correctly represented by the bond model.

It can be concluded for the three test series that the bond model gives a good representation of the experimentally obtained bond–slip curve. Both pull-out failure as splitting failure are correctly represented. The modelled curves lie within the experimental scatter.

7. Conclusions

This paper presented a two-phased FE model to obtain corrosion-dependent $\tau - \delta$ relations. The novelty of the modelling approach is that it consists of an enhanced 2D crack model that incorporates rust flow into pores and cracks; and a 3D bond model that can accommodate the strength increase for low corrosion levels. The combination of both models leads to a procedure that balances computational time and modelling detail. The model is validated on a substantial amount of experimental pull-out tests with varying corroded or bonded length and cover thickness among the test series. The following conclusions can be drawn:

- Incorporating the effect of the flow of corrosion products into the porous zone around the rebar and into corrosion-induced cracks is necessary to obtain representative crack widths. A percentage of the formed corrosion products is assumed to fill the cracks, and this percentage depends on the cover thickness.
- A novel approach is used in the crack model to incorporate the effect of confinement due to a different bonded length. This approach can be extended to include the confinement effect of stirrups.

Table 8
Overview of the modelling results of the bond model. For CL1 (TS2), the adopted friction angle (120% increase) is assumed.

Test series	Corrosion level	Average max. force (st. dev.) experiment [kN]	Max. force bond model [kN]
TS1	CL0	55.24 (1.26)	56.62
	CL2	35.10 (6.94)	41.98
	CL3	30.03 (3.23)	33.79
TS2	CL0	29.67 (3.64)	29.95
	CL1	58.78 (4.65)	53.02
	CL2	37.62 (0.70)	36.06
	CL3	36.15 (5.55)	33.32
TS3	CL0	28.27 (5.56)	29.22
	CL1	30.50 (1.76)	31.91
	CL2	44.85 (5.11)	42.49

- The developed crack model correctly represents the crack pattern and crack width as a function of corrosion level, bonded length, and cover thickness. Numerically obtained crack widths are within the experimental scatter. The sensitivity of two important parameters (the flow of corrosion products and confinement) were investigated, supporting the chosen values.
- Implementation of the corrosion crack by means of a crack interface as well as smeared concrete cracking in the 3D bond model allowed to properly simulate the shift from pull-out failure to splitting failure as well as the confinement of the concrete.
- By assuming a corrosion level-dependent friction angle, a good agreement between the numerical and experimental bond–slip curves is obtained for the test series and corrosion levels. For a large concrete cover and unbonded length, the increase in bond strength is significantly larger compared to the literature. An increase of the friction angle may be required to model such situation.

CRediT authorship contribution statement

C. Van Steen: Conceptualization, Methodology, Software, Validation, Formal analysis, Investigation, Data curation, Writing – original draft, Writing – review & editing, Funding acquisition. **T. Van Beirendonck:** Conceptualization, Methodology, Software, Validation, Formal analysis, Investigation, Writing – original draft. **R. Vrijdaghs:** Conceptualization, Methodology, Software, Writing – original draft. **M.A.N. Hendriks:** Conceptualization, Methodology, Resources, Writing – original draft. **E. Verstrynge:** Conceptualization, Methodology, Resources, Writing – original draft, Writing – review & editing, Supervision, Project administration, Funding acquisition.

Declaration of competing interest

The authors declare that they have no known competing financial interests or personal relationships that could have appeared to influence the work reported in this paper.

Data availability

Data will be made available on request.

Acknowledgements

This research was performed within the framework of project C24/17/042 "Multi-scale assessment of residual structural capacity of deteriorating reinforced concrete structures", supported by Internal Funds KU Leuven. Moreover, The financial support by Research Foundation Flanders (FWO) for the postdoctoral mandate of C. Van Steen (grant number 12ZD221N) is gratefully acknowledged.

The research described in this paper has been partially performed during a research stay of Charlotte Van Steen at TU Delft, the Netherlands. This stay was funded by Research Foundation Flanders (FWO) (grant number V405919N).

References

[1] Auyeung Y, Balaguru P, Chung L. Bond behavior of corroded reinforcement bars. ACI Mater J 2000;97(2):214–21.
[2] Fang C, Lundgren K, Chen L, Zhu C. Corrosion influence on bond in reinforced concrete. Cem Concr Res 2004;34:2159–67.
[3] Fédération international du béton (fib). Model code for concrete structures 2010. 2010.
[4] Lin H, Zhao Y, Feng P, Ye H, Ozbolt J, Jiang C, et al. State-of-the-art-review on the bond properties of corroded reinforcing steel bar. Constr Build Mater 2019;213:216–33.
[5] Yalciner H, Sensoy S. An experimental study on the bond strength between reinforcement bars and concrete as a function of concrete cover, strength and corrosion level. Cem Concr Res 2012;42:643–55.
[6] Wu Y-Z, Lv H-L, Zhou S-H, Fang Z-N. Degradation model of bond performance between deteriorated concrete and corroded deformed steel bars. Constr Build Mater 2016;119:89–96.
[7] Lin H, Zhao Y, Ozbolt J, Reinhardt HW. Bond strength evaluation of corroded steel bars via the surface crack width induced by reinforcement corrosion. Eng Struct 2017;152:506–22.
[8] Van Beirendonck T, Van Steen C, Verstrynge E. Experimental study of the bond degradation in concrete due to reinforcement corrosion. In: Proceedings of the 14th Fib PhD symposium in civil engineering. Rome, Italy: Federation for Structural Concrete; 2022, p. 475–82.
[9] Berto L, Simioni P, Saetta A. Numerical modelling of bond behaviour in rc structures affected by reinforcement corrosion. Eng Struct 2008;30:1375–85.
[10] Chernin L, Val DV, Cairns J. A new numerical model of the corroded steel-concrete interface. Mag Concr Res 2010;62(6):415–25.
[11] Lundgren K, Gylltoft K. A model for the bond between concrete and reinforcement. Mag Concr Res 2000;52(1):53–63.
[12] Lundgren K. Modelling the effect of corrosion on bond in reinforced concrete. Mag Concr Res 2002;54(3):165–73.
[13] Lundgren K. Bond between ribbed bars and concrete. part 1: Modified model. Mag Concr Res 2005;57(7):371–82.
[14] Lundgren K. Bond between ribbed bars and concrete. part 2: The effect of corrosion. Mag Concr Res 2005;57(7):383–95.
[15] Bolmsvik R, Lundgren K. Modelling of bond between three-wire strands and concrete. Mag Concr Res 2006;58(3):123–33.
[16] Michel A, Pease BJ, Peterova A, Geiker MR, Stang H, Thybo AEA. Penetration of corrosion products and corrosion-induced cracking in reinforced cementitious materials: Experimental investigations and numerical solutions. Cem Concr Compos 2014;47:75–86.
[17] Zandi Hanjari K, Lundgren K, Plos M, Coronelli D. Three-dimensional modeling of structural effects of corroding steel reinforcement in concrete. Struct Infract Eng 2013;9(7):702–18.
[18] Amleh L, Ghosh A. Modeling the effect of corrosion on bond strength at the steel-concrete interface with finite-element analysis. Can J Civil Eng 2006;33:673–82.
[19] Grassl P, Davies T. Lattice modelling of corrosion induced cracking and bond in reinforced concrete. Cem Concr Compos 2011;33(9):918–24.
[20] Van Steen C, Verstrynge E, Wevers M, Vandewalle L. Assessing the bond behaviour of corroded smooth and ribbed rebars with acoustic emission monitoring. Cem Concr Res 2019;120:176–86.
[21] American Society for Testing and Materials (ASTM). ASTM G1-03 standard practice for preparing, cleaning, and evaluation corrosion test specimens. 2011.
[22] Andrade C, Cesetti A, Mancinii G, Tondolo F. Estimating corrosion attack in reinforced concrete by means of crack opening. Struct Concr 2016;4:533–40.
[23] Caré S, Nguyen QT, L'hostis V, Berthaud Y. Mechanical properties of the rust layer induced by impressed current method in reinforced mortar. Cem Concr Res 2008;38:1079–91.
[24] Jaffer SJ, Hansson CM. Chloride-induced corrosion products of steel in cracked-concrete subjected to different loading conditions. Cem Concr Res 2009;39:116–25.
[25] Wong HS, Zhao YX, Karimi AR, Buenfeld NR, Jin WL. On the penetration of corrosion products from reinforcing steel into concrete due to chloride-induced corrosion. Corros Sci 2010;52:2469–80.
[26] Savija B, Lukovic M, Pacheco J, Schlangen E. Cracking of the concrete cover due to reinforcement corrosion: A two-dimensional lattice model study. Constr Build Mater 2013;44:626–38.
[27] Tran KK, Nakamura H, Kawamura K, Kunieda M. Analysis of crack propagation due to rebar corrosion using RBSM. Cem Concr Compos 2011;33:906–17.
[28] Liu Y, Weyers R. Modeling the time-to-corrosion cracking in chloride contaminated reinforced concrete. ACI Mater J 1998;95(6):675–81.
[29] Sola E, Ozbolt J, Balabanic G. Modelling corrosion of steel reinforcement in concrete: natural versus accelerated corrosion. In: Saouma V, Bolander J, Landis E, editors. Proceedings of the 9th international conference on fracture mechanics of concrete and concrete structures. 2016.
[30] Fischer C. Auswirkungen der bewehrungskorrosion auf den verbund zwischen stahl und beton [Ph.D. thesis], Universität Stuttgart; 2012.
[31] Liu M, Cheng X, Li X, Hu J, Pan Y, Jin Z. Indoor accelerated corrosion test and marine field test of corrosion-resistant low-alloy steel rebars. Case Stud Constr Mater 2016;5:89–99.
[32] Zhao Y, Ren H, Dai H, Jin W. Composition and expansion coefficient of rust based on X-ray diffraction and thermal analysis. Corros Sci 2011;53:1646–58.
[33] Shi J, Ming J. Influence of defects at the steel-mortar interface on the corrosion behavior of steel. Constr Build Mater 2017;136:118–25.
[34] Michel A, Pease BJ, Peterova A, Geiker MR. Experimental determination of the penetration depth of corrosion products and time to corrosion-induced cracking in reinforced cement based materials. In: Proceedings of ICDC (International congress on durability of concrete). 2012.
[35] Van Steen C, Pahlavan L, Wevers M, Verstrynge E. Localisation and characterisation of corrosion damage in reinforced concrete by means of acoustic emission and X-ray computed tomography. Constr Build Mater 2019;197:21–9.

[36] Rossi E, Polder R, Copuroglu O, Nijlang T, Savija B. The influence of defects at the steel/concrete interface for chloride-induced pitting corrosion of naturally-deteriorated 20-year-old specimens studied through X-ray computed tomography. Constr Build Mater 2020;235:117474.
[37] Bureau voor Normalisatie. NBN B 24-210: Proeven op metselstenen: Schijnbare volumemassa van de stof van de metselsteen. 1976.
[38] Sola E, Ozbolt J, Balabanic G, Mir ZM. Experimental and numerical study of accelerated corrosion of steel reinforcement in concrete: Transport of corrosion products. Cem Concr Res 2019;120:119–31.
[39] Andrade C, Anaya P. Advances in the description of corrosion induced cracking. In: Proceedings of the 2nd CACRS workshop capacity assessment of corroded reinforced concrete structure. 2021, p. 39–48.
[40] Thybo EA, Michel A, Stang H. Smeared crack modelling approach for corrosion-induced concrete damage. Mater Struct 2017;50(146):1–14.
[41] Zhao Y, Dai H, Jin W. A study of the elastic moduli of corrosion products using nano-indentation techniques. Corros Sci 2012;65:163–8.
[42] Molina FJ, Alonso C, Andrade C. Cover cracking as a function of rebar corrosion: part 2-numerical model. Mater Struct 1993;26(9):532–48.
[43] Michel A. Reinforcement corrosion: Numerical simulation and service life prediction [Ph.D. thesis], DTU; 2013.
[44] Toongoethong K, Maekawa K. Simulation of couped corrosive product formation, migration into crack and propagation in reinforced concrete sections. J Adv Concr Technol 2005;3(2):253–65.
[45] Ouglova A, Berthaud Y, François M, Foct F. Mechanical properties of an iron oxide formed by corrosion in reinforced concrete structures. Corros Sci 2006;48:3988–4000.
[46] Michel A, Otieno M, Stang H, Geiker MR. Propagation of steel corrosion in concrete: Experimental and numerical investigations. Cem Concr Compos 2016;70:171–82.
[47] DIANA FEA. Diana 10.5 user's manual. 2021.
[48] Castorena-Gonzalez JH, Martin U, Gaona-Tiburcio C, Nunez-Jaquez RE, Almeraya-Calderon JM, Bastidas DM. Modeling steel corrosion failure in reinforced concrete by cover crack width 3d fem analysis. Front Mater 2020;7:41. http://dx.doi.org/10.3389/fmats.2020.00041.
[49] Mak MWT, Desnerck P, Lees JM. Corrosion-induced cracking and bond strength in reinforced concrete. Constr Build Mater 2019;208:228–41.
[50] Torres-Acosta AA, Sagues AA. Concrete cracking by localized steel corrosion - geometric effects. ACI Mater J 2004;101(6):501–7.
[51] Lundgren K. Effect of corrosion on the bond between steel and concrete: an overview. Mag Concr Res 2007;59(6):447–61. http://dx.doi.org/10.1680/macr.2007.59.6.447.
[52] Bazant ZP, Pfeiffer PA. Shear fracture tests of concrete. Mater Struct 1986;19:111–21.